Solubility and solution mechanisms of chlorine and fluorine in aluminosilicate melts at high pressure and high…

Article *in* American Mineralogist · October 2015

DOI: 10.2138/am-2015-5201

CITATIONS
5

READS
55

4 authors, including:

Celia Dalou
Centre de Recherches Pétrographiques et …
28 PUBLICATIONS **146** CITATIONS
SEE PROFILE

Charles Le Losq
Australian National University
37 PUBLICATIONS **178** CITATIONS
SEE PROFILE

American Mineralogist, Volume 100, pages 2272–2283, 2015

AMORPHOUS MATERIALS: PROPERTIES, STRUCTURE, AND DURABILITY

Solubility and solution mechanisms of chlorine and fluorine in aluminosilicate melts at high pressure and high temperature†

Celia Dalou[1,*], Charles Le Losq[1], Bjorn O. Mysen[1] and George D. Cody[1]

[1]Geophysical Laboratory, Carnegie Institution of Washington, 5251 Broad Branch Road, NW, Washington D.C., U.S.A.

Abstract

The solubility and solution behavior of F and Cl in peralkaline aluminosilicate compositions in the systems Na_2O-Al_2O_3-SiO_2 and K_2O-Al_2O_3-SiO_2 have been determined for glasses quenched from melts equilibrated at 1400 and 1600 °C in the 1.0–2.5 GPa pressure range. With Al/(Al+Si) increasing from 0 to 0.33 in sodium aluminosilicate melts, F solubility (saturation concentration) increases from 3.3 to 7.4 mol%, whereas Cl solubility decreases from 5.7 to 2.5 mol%. There is no difference in F solubility in sodium or potassium aluminosilicate melts. However, the Cl solubility in potassic aluminosilicate melts is 40–60% lower than in sodic melts with the same Al/(Al+Si) and Na or K mole fraction.

Fluorine depolymerizes the silicate melt structure and forms Si-F, Al-F, and Na-F complexes, the proportion of which depends on the melt Al/(Al+Si) ratio. Dissolution of Cl results in a small degree of depolymerization of Al-free silicate melt, whereas Cl has a polymerizing effect in aluminosilicate melts. In both cases, formation of Na-Cl complexes appears to be the driving solution mechanism.

The differences in F and Cl solution mechanisms result in contrasting depolymerizing effects that become more pronounced with increasing degree of magmatic differentiation. Through such modifications of melt structure, F and Cl have significant effects on magma properties such as viscosity, compressibility, and element partitioning.

Keywords: Fluorine, chlorine, solubility, solution mechanism, aluminosilicate melt, ionic complexes, magma degassing

Introduction

Because of their effects on magma properties, F and Cl are of particular interest for assessing the dynamics of volcanic systems. They can be used as geochemical tracers that allow us to reconstruct the eruptive dynamics of volcanic edifices, as shown for instance by the study of Villemant and Boudon (1998) focused on Mt Pelée (Martinique, French West Indies) or by the study of Balcone-Boissard et al. (2011) focused on the 79 AD eruption of Vesuvius (Italy). Therefore, knowledge of the solubility and bonding of F and Cl in silicate melts and associated effects on melt structure is of prime importance for geochemical and volcanological problems.

Fluorine and chlorine concentration in magmatic liquids (≤1 wt%) is low compared to H_2O in magmas, yet the halogens can play a significant role during magmatic processes. Dissolved F lowers silicate melt viscosity (Dingwell 1987, 1989; Dingwell et al. 1993; Dingwell and Hess 1998; Giordano et al. 2004) and crystallization temperatures (Wyllie and Tuttle 1961; van Groos and Wyllie 1968; Luth 1988a; Filiberto et al. 2012) in a manner resembling H_2O. Our understanding of the effect of Cl on melt properties is considerably less comprehensive. A few studies exist on the effect of Cl on melt physical properties (e.g., Dingwell and Hess 1998; Zimova and Webb 2006, 2007) and its effect on liquidus temperatures (Filiberto and Treiman 2009). Chlorine dissolved in peralkaline melt can increase viscosity, but it reduces the liquidus temperature.

The type of fluoride complexes formed in melts determines how F affects silicate melt structure. Results from Raman, infrared, and ^{19}F nuclear magnetic resonance (NMR) spectroscopy suggest that F could form Si-F bonds when dissolved in SiO_2 melts (Dumas et al. 1982; Duncan et al. 1986). However, as the concentration of Al and alkalis or alkaline earth elements increases, F can also form Al-F bonds as well as alkali or alkaline earth fluoride complexes (Mysen and Virgo 1985a, 1985b; Foley et al. 1986; Luth 1988b). Recent data from ^{19}F and ^{29}Si magic angle spinning (MAS) NMR spectroscopy for Na-aluminosilicate quenched melts (glasses) have suggested that Na-F and Al-F complexing (with variable Al coordination and variable Si/Al ratio in the F-bearing complexes) is more important than complexes with Si-F bonding (Kohn et al. 1991; Schaller et al. 1992; Stebbins and Zeng 2000; Zeng and Stebbins 2000; Stebbins et al. 2000; Mysen et al. 2004).

For Cl-bearing melts, both viscosity measurements (Dingwell and Hess 1998; Zimova and Webb 2006, 2007; Baasner et al. 2013) and structural data from ^{35}Cl MAS NMR spectroscopy (Stebbins and Du 2002; Sandland et al. 2004; Evans et al. 2008) indicate that Cl preferentially bonds with network modifiers (alkalis and/or alkaline earths). Such solution mechanisms imply that Cl causes silicate melt polymerization and, consistently, dissolution of Cl in peralkaline melts increases their viscosity. However, dissolved Cl produces the opposite effect

* E-mail: cdalou@umn.edu

† Special collection papers can be found on GSW at http://ammin.geoscienceworld.org/site/misc/specialissuelist.xhtml.

0003-004X/15/0010–2272$05.00/DOI: http://dx.doi.org/10.2138/am-2015-5201

on the viscosity of peraluminous melts, which decreases upon Cl addition (Baasner et al. 2013). This difference suggests that the effect of Cl on melt structure depends on melt composition. Different solution mechanisms of F and Cl are also reflected by different diffusivity of F and Cl in magmatic melts (Alleti et al. 2007; Balcone-Boissard et al. 2009; Böhm and Schmidt 2013). Indeed, F diffuses one order of magnitude faster than chlorine in phonolitic melts (Balcone-Boissard et al. 2009; Böhm and Schmidt 2013), whereas in basaltic melts, F diffusion is half as fast as Cl (Alleti et al. 2007).

Despite the important and different effect of F and Cl on properties of magmatic melts, little or no systematic efforts have been made to compare their solubility and solution mechanisms in silicate and aluminosilicate melts of similar compositions at similar pressure and temperature conditions. We report here results from experiments on F and Cl solubility and solution mechanisms in peralkaline and meta-aluminous quenched melts in F- or Cl-enriched Na_2O-Al_2O_3-SiO_2 and K_2O-Al_2O_3-SiO_2 systems.

METHODS

Experimental methods

Two different sets of starting materials were prepared, one on the joins Na_2O-SiO_2 and $NaAlO_2$-SiO_2 and the second on the joins K_2O-SiO_2 and $KAlO_2$-SiO_2. The F and Cl were added to these starting compositions in the experimental sample container.

Compositions of starting materials are shown in Table 1. In Al-free systems, the NS5 and KS5 compositions used for F solubility experiments stand for $Na_2O{\cdot}SiO_2$ and $K_2O{\cdot}5SiO_2$, respectively. The NS3 and KS3 compositions used for Cl solubility experiments stand for $Na_2O{\cdot}3SiO_2$ and $K_2O{\cdot}3SiO_2$, respectively. The NS4 composition used for both F and Cl solubility experiments denotes $Na_2O{\cdot}4SiO_2$. The aluminum-bearing compositions are denoted NS3Ax, KS3Ax, NS4Ax, NS5Ax, and KS5Ax, in which x represents the mole percent Al_2O_3, which varied from 2.5 to 12.5. The studied melts are peralkaline (i.e., M/Al > 1, with M = Na or K), such that Al^{3+} can be considered as exclusively in fourfold coordination in fully polymerized Q^4 units charged balanced by the alkalis (see, for example, Mysen and Richet 2005, chapter 4, for review of the concepts of charge-balance of tetrahedrally coordinated Al^{3+}, and Mysen et al. 2003, for experimental data on Al^{3+} distribution among Q-species in peralkaline aluminosilicate melts). To isolate the potential effects of Al/(Al+Si) from changes in melt polymerization, the aluminosilicate compositions were synthesized such that the non-bridging oxygen per tetrahedron

TABLE 1. Composition of starting glasses (wt%)[a]

	NS3A0 [13] $PdCl_2$	NS3A2.5 [16] $PdCl_2$	NS3A5 [12] $PdCl_2$	NS3A7.5 [13] $PdCl_2$	NS3A10 [12] $PdCl_2$	NS3A12.5 [18] $PdCl_2$
SiO_2	75.96(57)	69.90(20)	64.98(62)	57.89(45)	52.41(31)	46.80(43)
Al_2O_3	–	4.55(6)	7.84(10)	12.08(13)	15.86(19)	18.99(28)
Na_2O	23.75(70)	26.31(15)	28.06(28)	30.90(32)	32.09(37)	33.95(33)
Total	99.71	100.77	100.89	100.87	100.36	99.74
Al/(Al+Si)[b]	0	0.07(0.3)	0.12(1)	0.20(1)	0.26(1)	0.32(1)
NBO/T[c]	0.61	0.61	0.61	0.63	0.61	0.63
	NS5A0 [12] AgF_2	NS5A2.5 [13] AgF_2	NS5A5 [12] AgF_2	NS5A7.5 [12] AgF_2	NS5A10 [13] AgF_2	NS5A12.5 [11] AgF_2
SiO_2	83.84(41)	76.18(56)	70.17(79)	64.45(91)	59.49(68)	51.01(69)
Al_2O_3	–	4.96(17)	9.14(20)	11.95(84)	15.54(81)	20.91(48)
Na_2O	16.34(16)	19.32(28)	21.51(60)	23.49(23)	24.84(72)	27.65(56)
Total	100.18	100.45	100.81	99.99	99.87	99.58
Al/(Al+Si)	0	0.07(1)	0.13(2)	0.18(2)	0.24(2)	0.33(1)
NBO/T	0.38	0.39	0.38	0.40	0.38	0.38
	KS3A0[d] [12] $PdCl_2$	KS3A2.5[d] [12] $PdCl_2$	KS3A5[d] [12] $PdCl_2$	KS3A7.5[e] [12] $PdCl_2$	KS3A10[e] [12] $PdCl_2$	
SiO_2	67.34	60.80	55.12	46.95(36)	39.80(40)	
Al_2O_3	–	3.54	7.09	12.17(16)	16.48(11)	
K_2O	33.2	35.36	37.65	41.29(16)	43.91(13)	
Total	100.56	99.7	99.86	100.41	100.19	
Al/(Al+Si)	0	0.06	0.13	0.23(1)	0.33(1)	
NBO/T	0.63	0.63	0.63	0.63	0.62	
	KS5A0 [12] AgF_2	KS5A2.5 [12] AgF_2	KS5A5 [11] AgF_2	KS5A7.5 [11] AgF_2	KS5A10 [12] AgF_2	
SiO_2	76.79(60)	68.94(53)	61.88(40)	57.37(41)	51.22(24)	
Al_2O_3	–	4.67(5)	9.00(10)	11.28(54)	14.33(9)	
K_2O	22.62(20)	26.29(19)	29.21(19)	30.73(52)	33.71(36)	
Total	99.41	99.90	100.09	99.38	99.26	
Al/(Al+Si)	0	0.07(1)	0.15(1)	0.19(1)	0.25(1)	
NBO/T	0.38	0.38	0.37	0.37	0.38	
	NS4A0 [12] AgF_2 or $PdCl_2$	NS4A5 [12] AgF_2 or $PdCl_2$	NS4A10 [11] AgF_2 or $PdCl_2$			
SiO_2	79.65(55)	68.16(43)	54.03(38)			
Al_2O_3	–	7.96(14)	17.21(32)			
Na_2O	19.74(21)	24.51(19)	29.37(29)			
Total	99.4	100.62	100.62			
Al/(Al+Si)	0	0.12(1)	0.27(1)			
NBO/T	0.48	0.49	0.49			

Notes: Numbers in brackets indicate number of individual electron microscope analyses included on average. Number in parentheses represents one standard deviation in terms of the least units cited.

[a] Operating conditions are presented in the text.

[b] Calculated from composition assuming that Si^{4+} and Al^{3+} are in tetrahedral coordination in the glasses. Error on Al/(Al+Si) calculated from oxide standard deviations.

[c] NBO/T calculated following Mysen and Richet (2005; Chapter 4). $NBO/T = (4{\cdot}X_T - 2{\cdot}X_O)/X_T$, where X_T and X_O are the atomic proportions of tetrahedrally coordinated cations (Si and Al) and oxygen, respectively.

[d] Theoretical composition, calculated from weighing (see text).

[e] Composition calculated from extrapolation to 0 s of variable counting times during SEM analysis (see text).

(NBO/T) ratio of the melts for a given compositional series does not change with increasing Al/(Al+Si) ratio of the bulk melt (Table 1).

Starting materials were prepared from mixtures of high-purity Na_2CO_3 or K_2CO_3, SiO_2, and Al_2O_3, decarbonated by slow heating (50 °C/15 min), and then melted for 2 h at ~100 °C above their liquidi (from 900 to 1400 °C; liquidus data from Osborn and Muan 1960). The melts were quenched to glass, crushed, and ground under alcohol for 1 h. Before grinding, one piece of glass of each composition was kept for major element analysis (Table 1). The heating step used for decarbonation was repeated before each experiment to prevent possible hydration or carbonation of the starting materials by absorption of CO_2 and H_2O from the ambient atmosphere. After this drying step, the powdered starting glasses were immediately loaded into Pt capsules with approximately 10 wt% F_2 (as 33 wt% AgF_2) or 5 wt% Cl_2 (as 23 wt% $PdCl_2$). The loaded capsules were welded shut before high-pressure and -temperature experiments.

Experiments were conducted at 1.0 to 2.5 GPa and 1400 °C for NS5Ax, KS5Ax, and NS4Ax compositions, and at 1600 °C for NS3Ax and KS3Ax compositions. A 90 min experimental duration was used for all experiments. This duration was chosen based on F and Cl diffusion data in basaltic melts [Alleti et al. (2007), accounting for pressure effects on diffusion, Dingwell et al. (1985)]. Experiments were performed in ¾ and ½ inch diameter furnace assemblies (Kushiro 1976) in a solid-media, high-pressure apparatus (Boyd and England 1960) at the Geophysical Laboratory (GL). Three 3 mm diameter capsules (4 mm length) were loaded in ¾ inch diameter furnace assemblies for 1.0, 1.5, and 2.0 GPa experiments; for 2.5 GPa experiments, a single 3 mm diameter capsule was loaded in ½ inch diameter furnace assemblies. From pressure-calibration with the quartz-coesite transition (Bohlen 1984), the uncertainty is ±0.1 GPa. The experimental temperature was controlled to within ±5 °C of the set point using $Pt/Pt_{90}Rh_{10}$ thermocouples. The samples were quenched by turning off the power to the furnace, which resulted in an initial (down to about 500 °C) average quenching rate of 100 °C/s.

After each experiment, the capsules were opened to recover the glass. A portion of the sample was retained for analysis by Raman spectroscopy. The remaining glass was mounted in epoxy resin and polished for analyses by energy-dispersive spectroscopy (EDS) on the scanning electron microscope (SEM).

Analytical methods

Major elements, F, and Cl were analyzed with a JEOL JSM-6500F field emission scanning electron microscope (FE-SEM) equipped with an energy-dispersive spectrometer (EDS) operating at 15 kV with a 0.1 nA beam current. A FE-SEM is more suitable than an electron microprobe for these analyses because the energy-dispersive spectrometer, in conjunction with the very low beam current of the FE-SEM, is useful for beam sensitive materials requiring low beam current during analysis (Raudsepp 1995). Although wavelength-dispersive spectrometer (WDS) analysis has been suggested to be more precise than EDS analysis for various analytical problems, the accuracy of both methods is comparable for polished glasses (Kuisma-Kursula 2000). Because our samples contain numerous bubbles (Fig. 1) and are very rich in Na and K, elements known to migrate under an electron beam, their analysis is challenging. These problems require use of a low beam current and a defocused electron beam to reduce Na and K migration. The shape and size of the beam area had to be adjusted for each analysis to avoid bubbles. The beam was defocused to 25 μm to reduce Na migration and to 25 to 50 μm to reduce K migration.

Pyrope (for Si), scapolite (for Na and Cl), ENAL20 (for Al, GL standard), K1597 (for K, NIST standard), topaz (for F), and MnO_2 (for Mn) were used as standards to obtain quantitative elemental analysis. Analytical accuracy and precision was evaluated by replicate measurements of orthoclase, diopside, and topaz of known compositions. Counting times used were 50 s per element.

To evaluate possible Na, K, F, or Cl loss, several analyses were carried out on the same sample spot. There were no significant compositional changes (within one standard deviation) for Na, F, or Cl, when using a beam larger than 15 × 15 μm^2, and for K when using a beam of 50 × 50 μm^2. However, significant losses were observed for the composition KS3Ax, even when the beam was defocused to 50 μm. For compositions KS3A7.5 and KS3A10, we time-monitored the K loss (counting times from 2 to 20 s) and extrapolated back to 0 s to deduce the initial K content. For KS3Ax compositions with $Al_2O_3 \leq 5$ mol%, K loss was so significant in the first 5 s that the extrapolation procedure could not be applied. Data presented in Table 1 for KS3, KS3A2.5, and KS3A5 were calculated, therefore, from the weighing data from the initial starting glass preparation.

Raman spectroscopy was employed to examine the structure of the quenched melts. The Raman instrument used is a JASCO model IRS-3100 confocal micro-Raman spectrometer with holographic gratings. Sample excitation was accomplished with the 532 nm line of a solid-state laser operating at a power of 6.4 mW on the sample. A 50× objective lens was employed for visual microscopic examination and spectroscopic analysis. Signal detection was provided by an Andor Model DV401-F1 1024 × 128 pixel (25 μm pixel size) Peltier-cooled CCD. A grating of 1200 grooves/mm was used, which results in a CCD window covering the 265–2110 cm^{-1} frequency range with resolution of ±3 cm^{-1}. Acquisition time was typically 15 min per spectrum.

Background correction of the Raman spectra was performed using a cross-validation spline function (Woltring 1986), fitted to spectral portions devoid of signals near 800 and 1300 cm^{-1}. After subtraction of the spline function, the 850 to 1300 cm^{-1} region was fitted using 5 to 6 Gaussian peaks with *lmfit* interface (Newville et al. 2014) and the optimization algorithms implemented in the Scipy library (Jones et al. 2001). During fitting, peak half widths were constrained to vary within ±20 cm^{-1} of their initial estimated value and peak frequencies were allowed to vary within ±25 cm^{-1}.

To avoid the under-constrained problem resulting from the strong convolution of signals from Q^3 and Q^4 units with similar intensities, we exploit the fact that Al^{3+} enters mostly in fully polymerized Q^4 units in peralkaline compositions (cf. Mysen et al. 2003; Allwardt et al. 2005; Le Losq et al. 2014). Mysen et al. (2003) showed that addition of Al at constant NBO/T should result in increasing contributions from Q^4 units; therefore, we expect little to no change in the half width of the peak assigned to Si-O stretch vibrations in Q^3 units (1050–1100 cm^{-1}; see Results and Discussion for peak assignments) with increasing Al/(Al+Si) at constant NBO/T. Furthermore, changes of the Na/Si ratio (and polymerization) should not significantly affect the half width of the 1050–1100 cm^{-1} peak assigned to Q^3. In the spectra of the Na_2O-SiO_2 glasses, it is ~32 cm^{-1} for Na/Si = 0.5 (this study), ~27 cm^{-1} for Na/Si = 0.67 (Le Losq et al. 2014) or ~29 cm^{-1} for Na/Si = 1.33 (Neuville 2006). For a given compositional series, we determined the half width of the 1050–1100 cm^{-1} peak in Al-free glasses, typically between 29 and 32 cm^{-1}, similar to reported values, and used this value to fit the spectra of Al-bearing glasses.

The curve-fitting itself was performed by minimizing the least-square difference between calculated and observed spectra using the Powell optimization algorithm (Powell 1964). After testing all gradient-based and gradient-less optimization algorithms implemented in Scipy, the Powell algorithm (a gradient-less method) gave the most robust and reproducible fits.

The errors on the estimated peak parameters were determined using the bootstrap method, well established for error estimation in statistics (cf. Efron and Tibshirani 1994). A three-step bootstrap technique was employed, which consists of (1) resampling the data, accounting for data uncertainty in the model errors; (2) randomly choosing between two optimization algorithms (Powell and

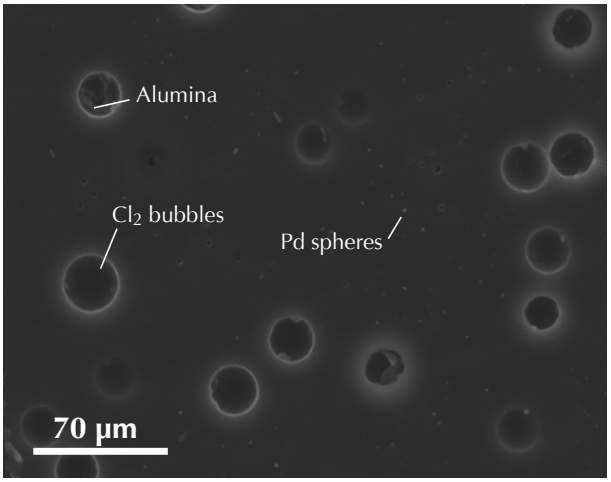

FIGURE 1. Backscattered electron image of C5NS3A5 sample. Chlorine saturation is indicated by the presence of bubbles from 5 to 35 μm in diameter. Traces of alumina suspension used for polishing are observed within the bubbles. Small white dots (<5 μm) are Pd_0 drops from the $PdCl_2 \rightarrow Pd_0+Cl_2$ decomposition. Fluorine samples look similar to chlorine samples, except that bubbles in F-bearing samples are smaller (nm to 5 μm in diameter) than in Cl-bearing samples.

Nelder-Mead [Nelder and Mead 1965]) for fitting the resampled data, accounting for the arbitrariness in the choice of the optimization algorithm and the precision and accuracy of that algorithm, and (3) twice fitting the resampled data with the chosen algorithm. The Nelder-Mead algorithm was chosen as the second algorithm because it provides results that are as robust as those from the Powell algorithm, but its reproducibility is slightly lower. Steps 1, 2, and 3 were repeated N times, and for each parameter, we calculated its standard deviation using its N values from the N models generated by the bootstrap. In this study, we used $N = 128$ because it was found that mean values and standard errors of the fitting parameters did not evolve significantly when $N > 80$.

Results and discussion

In the following sections, F and Cl solubility and solution behavior was determined with glasses. This glass structure reflects the structure of supercooled melt at the glass transition temperature.

At experimental conditions, F and Cl are released from the thermal decomposition of AgF_2 ($AgF_2 \rightarrow Ag_0+F_2$) and $PdCl_2$ ($PdCl_2 \rightarrow Pd_0+Cl_2$). At the end of the experiments, Ag_0 and Pd_0 are found as small, shiny beads of metal (nanometers to 3 μm), as also reported by Jago and Gittins (1989). The presence of these metal beads indicates that Ag and Pd were not oxidized during the experiments and do not bond with the melt structure. As the only volatiles present, F and Cl saturation in the melts is confirmed by the presence of bubbles. In the case of F-bearing samples, these bubbles were nanometers to 5 μm in diameter, whereas in the Cl-bearing samples, the bubbles were 10 to 40 μm in diameter (Fig. 1).

The F and Cl concentrations in the silicate and aluminosilicate quenched melts are presented in Tables 2 and 3. In these analyses, interference of some of the metal beads was unavoidable. The melt compositions were, therefore, renormalized to 100 wt% after subtraction of Ag and Pd contents in the analyses of the melts (up to 6 mol% of Ag and 0.78 mol% of Pd). Variation of Ag concentration (from 0 to 6 mol% between individual analytical points) resulted in a change smaller than 0.45 mol% in F, which is near or within one standard deviation of the F analysis. The compositional homogeneity of the quenched melts confirms that a duration of 90 min for the experiments was sufficient to achieve F and Cl equilibrium in melts (Table 2).

The F solubility increases from 3.33 (±0.73, 1σ) to 7.40 (±0.08) mol% in the NS5Ax sodic system, and from 3.63 (±0.23) to 6.52 (±0.55) mol% in the KS5Ax potassic system with increasing Al/(Al+Si) from 0.0 to 0.33 (Fig. 2a). The solubility in NS4Ax and NS5Ax melts is similar, within error. In comparison, in more polymerized melts such as that of $NaAlSi_3O_8$ composition [i.e., NBO/T ~ 0; Al/(Al+Si) = 0.25], the F solubility is 6–7 times greater (59 mol% F) at the same pressure and temperature conditions (Dingwell 1987).

In contrast to F, Cl solubility is negatively correlated with the bulk Al/(Al+Si) ratio of the melt (Fig. 2b). At 1.5 GPa and 1600 °C, with increasing Al/(Al+Si) from 0 to 0.33, the Cl concentration decreases from 5.70 (±0.65) to 2.45 (±0.30) mol% in the NS3Ax sodic system, and from 3.63 (±0.21) down to 1.14 (±0.20) mol% in the KS3Ax potassic system. The Cl solubility in Na-aluminosilicate melts, therefore, is about 1.5 times higher than that in K-aluminosilicate melts. The Cl solubility NS4Ax (1400 °C) and NS3Ax melts (1600 °C) are comparable (Fig. 2b), suggesting that neither slight changes in Na/Si nor a 200 °C temperature difference significantly affects Cl solubility, the latter observation being in agreement with Stagno and Dolejš (2007), Stelling et al. (2008), and Chevychelov et al. (2008). According to the model of Webster et al. (2015), a 200 °C temperature variation applied to our data should result in a 3% variation in Cl

Table 2. Run product compositions in mol% normalized to 100 mol% at 1.5 GPa

	F10NS5A0 [12]	F10NS5A2.5 [9]	F10NS5A5 [12]	F10NS5A7.5 [11]	F10NS5A10 [14]	F10NS5A12.5 [12]
			Solubility samples			
SiO_2	76.79(83)	73.88(61)	70.33(88)	64.40(48)	59.82(37)	48.28(66)
Al_2O_3		2.88(12)	5.21(10)	7.23(8)	10.08(11)	12.18(59)
Na_2O	19.88(23)	19.20(24)	20.16(31)	23.05(30)	23.79(11)	32.13(55)
F	3.33(73)	4.03(79)	4.29(36)	5.32(28)	6.31(37)	7.40(8)
	F10KS5A0 [10]	F10KS5A2.5 [15]	F10KS5A5 [11]	F10KS5A7.5 [13]	F10KS5A10 [11]	
SiO_2	79.46(61)	74.57(5)	69.70(5)	65.16(54)	60.81(47)	
Al_2O_3		2.97(9)	5.95(9)	7.35(10)	9.42(9)	
K_2O	17.18(8)	18.03(15)	19.25(16)	21.93(18)	23.23(16)	
F	3.36(23)	4.43(5)	5.10(57)	5.56(63)	6.52(55)	
	C5NS3A0[a] [12]	C5NS3A2.5 [15]	C5NS3A5 [10]	C5NS3A7.5 [10]	C5NS3A10 [12]	C5NS3A12.5 [13]
SiO_2	79.89(243)	72.53(138)	68.67(43)	66.21(42)	61.48(45)	53.44(79)
Al_2O_3		2.69(7)	5.03(3)	8.30(5)	11.10(16)	14.66(26)
Na_2O	14.41(62)	19.48(42)	22.36(26)	21.99(3)	24.32(26)	29.43(53)
Cl	5.70(65)	4.91(18)	3.94(66)	3.49(26)	3.09(38)	2.45(30)
	C5KS3A0[a] [11]	C5KS3A2.5[a] [12]	C5KS3A5[a] [10]	C5KS3A7.5 [12]	C5KS3A10 [12]	
SiO_2	85.45(62)	80.32(66)	76.58(83)	69.96(76)	61.55(62)	
Al_2O_3		2.76(7)	6.08(10)	8.85(12)	10.39(52)	
K_2O	10.92(21)	14.04(22)	15.04(30)	19.41(35)	26.92(252)	
Cl	3.63(21)	2.87(46)	2.30(47)	1.78(35)	1.14(20)	
	F10NS4A0 [12]	F10NS4A5 [12]	F10NS4A10 [12]	C5NS4A0 [12]	C5NS4A5 [12]	C5NS4A10 [11]
SiO_2	76.78(77)	66.06(174)	55.74(146)	80.42(126)	74.38(164)	60.26(105)
Al_2O_3		5.00(19)	11.44(33)		5.06(20)	11.50(74)
Na_2O	19.18(42)	23.88(132)	25.60(121)	15.12(87)	17.17(90)	25.76(183)
F & Cl	4.42(18)	5.06(41)	7.21(58)	4.46(9)	3.38(12)	2.48(13)

Notes: Numbers in brackets indicate number of individual electron microprobe analyses included on average. Numbers in parentheses represents one standard deviation in terms of the least units cited.

[a] Na_2O or K_2O loss during analysis.

Table 3. Run product compositions in mol% normalized to 100 mol% between 1 and 2.5 GPa

	F10NS5A0				F10NS5A5				F10NS5A10			
GPa	1[a]	1.5	2	2.5	1	1.5	2	2.5	1	1.5	2	2.5
SiO_2	85.49(94)	76.79(83)	80.16(172)	75.95(84)	72.71(32)	70.33(88)	71.40(38)	68.17(76)	57.67(69)	59.82(37)	57.25(69)	58.29(70)
Al_2O_3	–	–	–	–	5.37(16)	5.21(10)	5.38(13)	5.38(13)	11.43(42)	10.08(11)	11.18(41)	10.43(38)
Na_2O	11.59(3)	19.88(23)	15.66(14)	19.92(5)	17.84(9)	20.16(31)	17.53(18)	19.91(28)	25.24(101)	23.79(11)	24.85(99)	23.71(95)
F	2.91(39)	3.33(73)	4.19(66)	4.56(90)	4.08(31)	4.29(36)	5.69(79)	6.11(122)	5.65(17)	6.31(37)	6.72(20)	7.57(23)
	F10KS5A0				F10KS5A5				F10KS5A10			
GPa	1	1.5	2[a]	2.5	1	1.5	2	2.5	1	1.5	2	2.5
SiO_2	80.58(105)	79.46(61)	82.50(107)	81.58(20)	73.21(36)	69.70(5)	68.99(66)	69.92(41)	63.51(127)	60.81(47)	60.74(99)	61.28(60)
Al_2O_3	–	–	–	–	6.13(9)	5.95(9)	5.80(17)	6.02(1)	11.46(22)	9.42(9)	12.57(1)	10.29(18)
K_2O	16.99(86)	17.18(8)	13.92(88)	14.31(178)	16.14(271)	19.25(16)	19.07(165)	17.07(124)	19.13(110)	23.23(16)	22.38(262)	20.63(81)
F	2.43(42)	3.36(23)	3.58(61)	4.10(27)	4.51(10)	5.10(57)	6.14(51)	6.99(65)	5.79(29)	6.52(55)	7.24(33)	7.80(36)
	C5NS3A0				C5NS3A5				C5NS3A10			
GPa	1	1.5	2	2.5	1	1.5	2	2.5	1	1.5	2	2.5
SiO_2	78.10(172)	79.89(243)	78.55(151)	79.49(75)	71.18(58)	68.67(43)	70.38(39)	72.32(34)	61.39(59)	61.48(45)	61.29(88)	63.04(37)
Al_2O_3	–	–	–	–	5.11(18)	5.03(3)	5.01(12)	5.13(11)	11.05(27)	11.10(16)	11.09(38)	11.20(17)
Na_2O	18.67(39)	14.41(62)	14.40(57)	12.28(25)	20.18(45)	22.36(26)	19.53(43)	16.66(21)	24.66(37)	24.32(26)	23.66(35)	21.30(26)
Cl	3.23(11)	5.70(65)	7.05(106)	8.23(103)	3.42(28)	3.94(66)	5.08(34)	5.89(62)	2.89(11)	3.09(38)	3.94(64)	4.46(33)
	C5KS3A0				C5KS3A5				C5KS3A10			
GPa	1[a]	1.5[a]	2	2.5[a]	1	1.5	2	2.5	1	1.5	2	2.5
SiO_2	84.20(74)	85.45(62)	81.27(141)	84.79(49)	74.42(136)	76.58(83)	74.57(108)	74.58(100)	61.33(85)	61.55(62)	60.56(63)	60.45(127)
Al_2O_3	–	–	–	–	5.86(7)	6.08(10)	5.98(7)	6.29(12)	13.13(23)	10.39(52)	11.82(3)	11.87(13)
K_2O	12.84(10)	10.92(21)	14.71(20)	10.74(5)	17.63(100	15.04(30)	16.76(16)	16.16(4)	24.59(10)	26.92(252)	26.45(10)	26.23(11)
Cl	2.96(23)	3.63(21)	4.02(15)	4.46(33)	2.09(64)	2.30(47)	2.69(1)	2.97(14)	0.94(7)	1.14(20)	1.17(50)	1.46(93)

Notes: Number in parentheses represents one standard deviation in terms of the least units cited.
[a] Na_2O or K_2O loss during analysis.

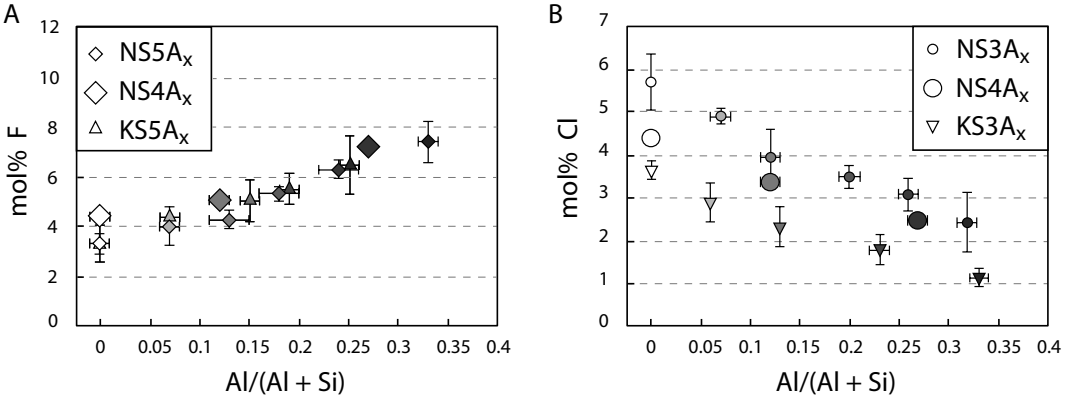

Figure 2. Solubility in mol% of F (**a**) and Cl (**b**) in aluminosilicate quenched melts as a function of their bulk Al/(Al+Si). All samples were equilibrated at 1.5 GPa. Samples F10NS5Ax, F10NS4Ax, F10KS5Ax, and C5NS4Ax were synthesized at 1400 °C and samples C5NS3Ax and C5KS3Ax were synthesized at 1600 °C. Error bars represent one standard deviation of the average of analyses of each sample (number of analysis are shown in brackets in Table 2). For F solubility experiments, diamonds refer to NS5Ax and NS4Ax samples and triangles to KS5Ax. For Cl-solubility experiments, circles refer to NS3Ax and NS4Ax samples and reversed triangles are KS3Ax samples. The grayscale represents the variation of the bulk melt Al/(Al+Si) ratio. The same color code is used in Figures 3 and 7. Large symbols are for NS4Ax samples measured by Raman spectroscopy and presented in Figures 3 and 7.

solubility, which is within the standard deviation on the present Cl solubility measurements.

The chlorine data are consistent with those of Zimova and Webb (2006) who also observed decreasing Cl solubility with increasing Al content in Na_2O-Fe_2O_3-Al_2O_3-SiO_2 melts. However, they are inconsistent with the empirical Webster et al. (2015) model, which predicts an increase of Cl solubility with Al/(Al+Si). This may arise from the fact that this empirical model was developed on the basis of Cl solubility data in chemically much more complex natural systems. Indeed, results from the model are consistent with a Cl solubility increase from felsic [latite; NBO/T = 0.11; Al/(Al+Si) = 0.25] to mafic [basaltic; NBO/T = 0.76; Al/(Al+Si) = 0.27] melts, as observed by Webster and De Vivo (2002). Therefore, Cl solubility is probably a complex function of the melt composition.

There is a linear, positive relationship between pressure and both F and Cl solubility (Fig. 3). While the F solubility-dependence on pressure is the same regardless of the Al content (Fig. 3a), the Cl solubility-dependence is about three times higher in Al-free and Al-poor (NS3, NS3A5 and KS3, KS3A5) melts than in Al-rich melts (Fig. 3b). Moreover, the pressure dependence of Cl solubility is about three times greater in NS3Ax melts than in KS3Ax melts (Fig. 3b).

Raman spectroscopy of F- and Cl-bearing sodic melts

Raman spectra of volatile-free and of F- or Cl-bearing NS4Ax quenched melts in the frequency range of first-order Raman scattering of (Si, Al)-O stretch vibrations are shown in

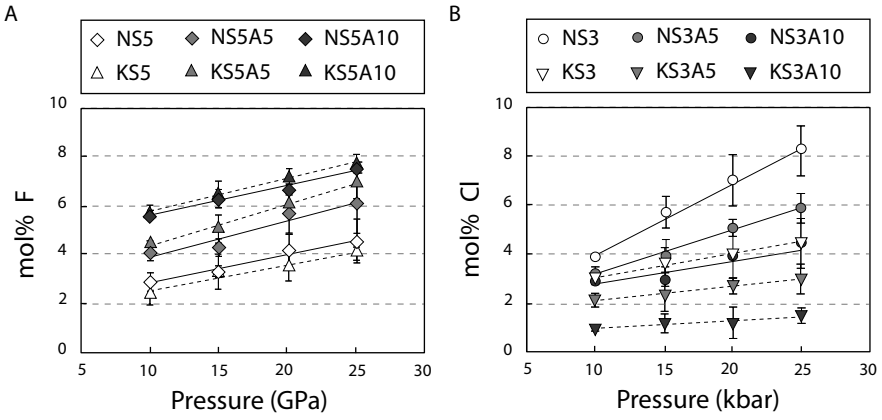

Figure 3. Solubility variation of F (**a**) and Cl (**b**) as a function of pressure. Symbols are the same as in Figure 2. Solid lines show F and Cl solubility dependence in the sodic systems, and dashed lines in the potassic systems. Samples NS5Ax, KS5Ax, and NS4Ax were synthesized at 1400 °C and samples NS3Ax and KS3Ax at 1600 °C. Both F and Cl solubility increase with increasing pressure from 1.0 to 2.5 GPa. The relation of Cl solubility with pressure appears to depend on melt composition as shown by the Cl vs. pressure slopes varying with the bulk melt Al/(Al+Si) ratio. In contrast, the F solubility dependence with pressure does not vary, or not significantly, with the bulk melt Al/(Al+Si) ratio, but its dependence is higher in the potassic system than in the sodic systems.

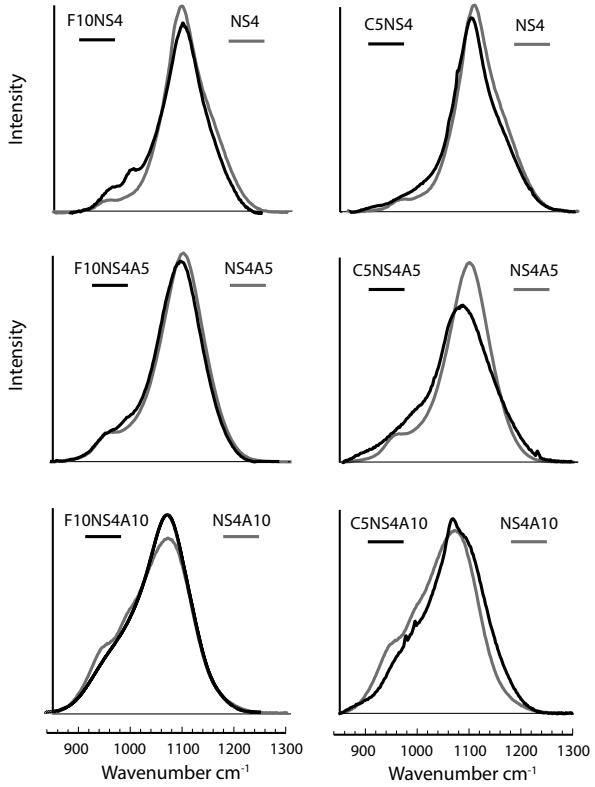

Figure 4. Raman spectra between 850 and 1300 cm^{-1} obtained for volatile-free samples (in gray) and in volatile-bearing (F- and Cl-bearing) samples (in black). Spectra, volatile-free or volatile-bearing, are normalized to have the same area.

Figure 4 (between 850 and 1300 cm^{-1}). Note that the spectra are reproducible in each sample regardless of the presence and abundance of metal beads. Therefore, we conclude that the presence of metal beads have no influence on the melt structure. There is a maximum between 1000 and 1100 cm^{-1} with visible shoulders on both sides, the detailed features of which vary with Al/(Al+Si). This spectral topology resembles the Raman spectra of volatile-free peralkaline aluminosilicate melts (Merzbacher and White 1991; Mysen et al. 2003). However, Raman spectra of F- or Cl-bearing melts differ from spectra of volatile-free melt. In Al-free and Al-poor compositions, both F- and Cl-bearing melts show Raman spectra with more intensity near 950–1000 cm^{-1} and less intensity near 1100 and 1150 cm^{-1} compared to Raman spectra of volatile-free melts. In Al-rich melts, less intensity near 950–1000 cm^{-1} and more intensity near the 1100 and 1150 cm^{-1} are observed in the spectra of both F- and Cl-bearing glasses compared to those of volatile-free glasses. To decipher those topological differences, Raman spectra were deconvoluted with 5 to 6 bands, in agreement with previous studies on similar melt compositions (Mysen et al. 2003; Le Losq et al. 2014; Dalou and Mysen 2015).

The assignments of bands in the 850–1300 cm^{-1} region of the Raman spectra have been extensively described to be associated with (Si,Al)-O stretch vibrations (e.g., Mysen et al. 1982; McMillan 1984; Matson et al. 1986; Mysen 1999; Le Losq et al. 2014). In this study, we assigned the main bands in the 850–890, 930–970, 1070–1110, and 1100–1170 cm^{-1} ranges in accord with Mysen et al. (2003) and Le Losq et al. (2014), who supported the Raman assignments with NMR spectroscopic data. Details on band location, bandwidth, and amplitude are presented in Table 4.

The band near 950 cm^{-1} (dark gray shading in Fig. 5) is assigned to Si-O stretching vibrations in Q^2 structural units, the band near 1100 cm^{-1} (gray shading in Fig. 5) to Si-O stretching vibrations in Q^3 units and the bands near 1150 and 1190 cm^{-1} (white bands in Fig. 5) to stretching of (Si,Al)-O° (O°: bridging oxygen) bonds in Q^4 units. Consistent with Mysen et al. (1982), Seifert et al. (1982), Mysen (1990), Neuville and Mysen (1996), Le Losq and Neuville (2013), and Le Losq et al. (2014), a bimodal shape is observed for the Si-O stretch signal assigned to

TABLE 4. Parameters resulting from Raman spectra deconvolutions: Raman shift (cm^{-1}), full-width at half maximum height (FWHM, cm^{-1}), and intensity

	NS4	NS4A5	NS4A10	F10NS4	F10NS4A5	F10NS4A10	C5NS4	C5NS4A5	C5NS4A10
Raman shift									
890 band[a]	–	–	–	–	–	–	905(2)	894(6)	882(3)
Q^2	957(0.1)	966(2)	945(2)	957(1)	964(2)	973(6)	990(4)	962(19)	949(6)
Si-F	–	–	–	993(0.5)	1000(2)	1001(9)	–	–	–
Si-O°	1046(0.3)	1049(4)	1006(3)	1049(1)	1052(3)	1027(7)	1050(0.6)	1010(8)	1005(5)
Q^3	1098(0.5)	1090(4)	1051(4)	1099(1)	1089(3)	1064(6)	1095(0.4)	1068(2)	1057(3)
$Q^{4,II}$	1148(1)	1117(6)	1190(3)	1145(2)	1117(3)	1098(5)	1146(1)	1110(1)	1098(3)
$Q^{4,I}$	1181(6)	1156(8)	1143(4)	1183(5)	1151(5)	1148(12)	1171(4)	1157(6)	1147(6)
[b]CO_3^{2-}	–	–	–	–	–	1065(1)	–	–	1063(0.5)
FWHM									
890 band[a]	–	–	–	–	–	–	28(2)	15(6)	20(2)
Q^2	29(0.4)	39(1)	37(1)	31(1)	37(1)	51(3)	41(2)	42(13)	40(6)
Si-F	–	–	–	15(0.4)	20(3)	15(0.1)	–	–	–
Si-O°	35(1)	36(0.1)	33(3)	37(2)	35(4)	32(3)	31(3)	34(9)	44(4)
Q^3	31(0.5)	30(0.1)	30(0.1)	30(0.5)	30(0.1)	30(0.1)	30(1)	32(0.1)	32(0.1)
$Q^{4,II}$	25(2)	34(4)	35(2)	26(2)	29(1)	37(3)	23(1)	32(2)	34(2)
$Q^{4,I}$	32(2)	37(4)	44(1)	27(3)	34(2)	43(2)	38(2)	41(2)	40(2)
[b]CO_3^{2-}	–	–	–	–	–	–	–	–	9(0.3)
Intensity									
890 band[a]	–	–	–	–	–	–	2(0.1)	2(1)	3(1)
Q^2	5(0.1)	14(0.3)	32(2)	13(0.1)	15(0.5)	19(2)	10(1)	13(6)	14(4)
Si-F	–	–	–	10(1)	7(2)	2(1)	–	–	–
Si-O°	20(0.5)	34(4)	48(4)	37(1)	41(3)	16(3)	23(1)	22(5)	37(3)
Q^3	93(1)	51(11)	48(5)	85(3)	58(8)	32(4)	91(1)	73(6)	49(4)
$Q^{4,II}$	29(5)	48(8)	73(6)	31(2)	38(5)	31(3)	19(3)	54(3)	61(5)
$Q^{4,I}$	18(3)	15(5)	13(2)	13(2)	22(4)	5(4)	22(2)	30(2)	23(3)
[b]CO_3^{2-}	–	–	–	–	–	–	–	–	10(1)

Notes: Number in parentheses represents one standard deviation in terms of the least units cited. [a] See assignment discussion in the text. [b] Contamination, see Figure 5.

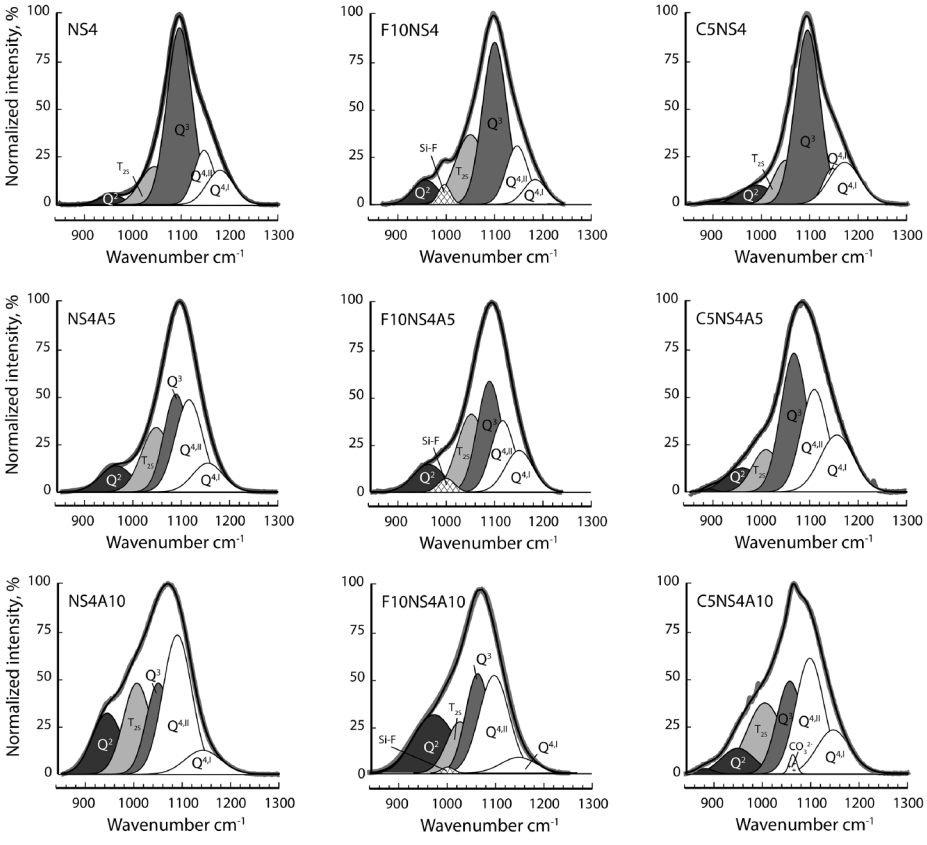

FIGURE 5. Examples of curve-fitted Raman spectra of melts in the frequency region of (Si, Al)-O stretch vibrations for compositions indicated on each plot. The spectra are normalized to 100% intensity. The individual lines are of Gaussian shape and fitted to the spectra as discussed in the text. Peaks near 900, 950, 1100, 1150, and 1180 cm^{-1} Raman spectra are related to (Si, Al)-O stretching in Q^2, Q^3, $Q^{4,II}$, and $Q^{4,I}$ tetrahedral units. See text for discussion of band assignments. The 1000–1070 cm^{-1} peak is related to the stretching T_{2s} vibrational mode of SiO_2 units as explained in the test.

Q^4 units. Two Gaussians, here named $Q^{4,II}$ (1140 cm^{-1}) and $Q^{4,I}$ (1170 cm^{-1}), are used as a mathematical solution to account for this asymmetry of the Si-O stretch signal from Q^4 units (see Le Losq et al. 2014 for further discussion). In contrast, Dalou and Mysen (2015) used only one Gaussian to describe Q^4 units; their approach was chosen to facilitate comparison to the data of Mysen (2007). There is, therefore, an expected discrepancy between the Raman fit results of the present study and Dalou and Mysen (2015). However, we chose use two Gaussians for fitting the Q^4 signal, since it is clearly assymetric in pure silica, silica-rich silicate glasses, and tectosilicate glasses. (Mysen et al. 1982; Seifert et al. 1982; Mysen 1990; Neuville and Mysen 1996; Le Losq and Neuville 2013; Le Losq et al. 2014; Neuville et al. 2014).

A band around 1000–1070 cm^{-1} is observed in all spectra (light gray shading). Results from molecular simulations (Spiekermann et al. 2012, 2013) and comparisons of simulations and neutron scattering data (Sarnthein et al. 1997; Pasquarello et al. 1998) with Raman data (Le Losq and Neuville 2013; Le Losq et al. 2014) indicate that this peak may be assigned to the Si-O asymmetric stretching vibrational mode of SiO_2 tetrahedra. Those studies show that this peak probably arises from asymmetric stretching of Si-O bonds in Q^n units and clearly establish that the Si-O asymmetric stretching mode T2 of SiO_2 tetrahedra occur at similar frequencies (Sarnthein et al. 1997; Pasquarello et al. 1998). This band is however difficult to fit, because it is present in a region in the spectra that is not well defined, i.e., where no significant shoulders or peaks are present. Our results show that its intensity and width increase with increasing Al content, consistently with Le Losq et al. (2014). The width is not significantly changing (±5 cm^{-1}), compared to changes observed in tectosilicate glasses (Neuville and Mysen 1996; Le Losq and Neuville 2013).

In Raman spectra of Cl-bearing glasses, a band near 890 cm^{-1} was necessary to fit the spectra. It may be assigned to (Si,Al)-O^- (O^-: non-bridging oxygen) vibrations in Q^1 structural units (cf. Mysen et al. 1982), but the origin of this peak is uncertain. This peak is barely visible in the spectra, and will be put aside for quantification of the glass polymerization using the area of the Q^n peaks.

The curve-fitting of the spectra of F-bearing quenched melts requires an additional band around 990 cm^{-1} (cross-hatched in Fig. 5) to minimize the χ^2 (Table 5). The peak was not observed in spectra of silicate melts with low-F content [F/(F+O) ≤ 0.015], but appears at F/(F+O) > 0.02 (e.g., Mysen and Virgo 1985a, 1985b; Luth 1988b; Mysen et al. 2004). This band is not required in curve-fits of the Raman spectra of halogen-free or Cl-bearing melts. Therefore, it likely can be assigned to a vibration involving F. It may not be assigned to Na-F, because such molecules gives Raman signals near 450–500 cm^{-1} (e.g., Hardy et al. 1969). A band at ~945 cm^{-1} was observed in SiO_2-F glasses and was assigned to Si-F stretching vibrations in SiO_3F tetrahedral units on the basis of valence force field calculations (Dumas et al. 1982).

TABLE 5. Comparison of χ^2 from fits to F-bearing NS4Ax melts

	χ^2 w/ 990 cm^{-1} band	χ^2 w/o 990 cm^{-1} band
F10NS4	2.6	15.8
F10NS4A5	22.0	18.6
F10NS4A10	5.4	10.5

A peak observed near 907 cm^{-1} was assigned to Si-F stretching vibrations in amorphous fluorinated silicon films (Yamamoto et al. 1983). Fluorine-19 NMR data of F-bearing silicate glasses have provided evidence of SiO_3F and SiO_2F_2 complexes, but not of SiF_4 and $SiOF_3$ (Duncan et al. 1986). Therefore, the band near 990 cm^{-1} observed in our F-saturated silicate and aluminosilicate melts can be assigned to stretching vibrations of Si-F bonds. In agreement with Dumas et al. (1982), we propose that those bonds occur in SiO_3F tetrahedral units, where fluorine replaces one of the O atoms in the silicate tetrahedral. It is difficult to assess the exact degree of polymerization of the oxygen atoms in the SiO_3F units. Changing the BO/NBO ratio of the SiO_3F units is likely to result in changing the Si-F frequency in such unit (Mysen and Virgo 1985b). However, we note that the vibrational frequency of the 990 cm^{-1} band is constant, regardless of the Al/(Al+Si) of the present glasses (Table 6). Therefore, the exact extent to which the oxygen forms bridges with neighboring silicate tetrahedra in the SiO_3F units does not change with Al/(Al+Si).

To quantify the effect of F and Cl on the silicate melt structure, relative band intensities from the Raman spectra must be converted into Q^n-species units fractions through (Mysen 1990; Mysen and Frantz 1993)

$$[Q^n] = \theta^n \times A_{Qn} \quad (1)$$

where θ^n is a conversion factor, depending directly on the Raman cross section of Si-O bonds in Q^n units. In addition, melt polymerization can be calculated using the mean number of non-bridging oxygen per tetrahedrally coordinated cation (NBO/T; here Al^{3+} and Si^{4+}):

$$\text{NBO/T} = 2 \times [Q^2] + [Q^3] = 2 \times [\theta^2 \times A_{Q2}] + [\theta^3 \times A_{Q3}] \quad (2a)$$

Comparison of NBO/T between F- or Cl-bearing melts and volatile-free melts can be obtained by:

$$\Delta\text{NBO/T} = \text{NBO/T}_{\text{F or Cl}} - \text{NBO/T}_{\text{volatile-free}} \quad (2b)$$

The θ^2 and θ^3 values are close to unity for sodium silicates (Mysen 2007), therefore θ^2 and θ^3 factors are negligible in Equation 2a. Therefore, we can calculate a Raman-apparent ΔNBO/T with Equation 2b with using directly the Raman areas. This Raman-apparent ΔNBO/T will be close to the true ΔNBO/T based on the assumption that θ^n factors are negligible. Whether or not

TABLE 6. Species abundance from Raman spectra of melts

	Relative peak area			ΔNBO/T
	Q^2	Q^3	[a]Q^4	
NS4	0.04(0.2)	0.67(4)	0.30(11)	–
NS4A5	0.12(2)	0.36(9)	0.52(28)	–
NS4A10	0.20(2)	0.25(3)	0.55(9)	–
F10NS4	0.10(1)	0.62(10)	0.29(9)	0.33(10)
F10NS4A5	0.13(2)	0.42(9)	0.44(14)	0.20(9)
F10NS4A10	0.29(5)	0.29(6)	0.42(35)	0.23(8)
C5NS4	0.09(1)	0.62(12)	0.28(4)	0.33(12)
C5NS4A5	0.09(7)	0.40(9)	0.51(16)	0.10(12)
C5NS4A10	0.11(4)	0.30(5)	0.59(9)	0.03(7)

Notes: Errors on Q^n species abundances were recalculated following the method of Mysen (2007). To calculate the Q^n-species mole fractions, the area of bands around 990, 1010–1050, and 1065 cm^{-1} were not taken into account.
[a] Sum of $Q^{4,I}$ and $Q^{4,II}$.

halogen substitution affects the integrated intensities of Raman bands assigned to Si-O stretch vibrations is not known. By using θ^n-factors determined from halogen-free melts, we might have introduced an unknown inaccuracy in the calculated Q^n fractions in halogen-bearing melts. Although Cl and F may have a slight effect on θ^n factors, it is not significant enough to influence the rest of the discussion.

F solution mechanisms

Fluorine in Al-free melts. The F-bearing NS4 silicate glass has fewer Q^3 and Q^4 and more Q^2 units than the halogen-free NS4 glass, which translates to higher Raman-based NBO/T-values (Fig. 6). The dominant complexes in Na_2O-SiO_2-F melts, inferred from ^{19}F and ^{29}Si NMR spectroscopy, have been reported to be Na-F complexes (e.g., Schaller et al. 1992; Mysen et al. 2004). The observed depolymerizing effect of F (Fig. 6) is inconsistent with the dominance of (Na+F)-bearing complexes. If this were the only fluorine solution mechanism, the silicate melt would become more polymerized (Raman-based NBO/T decreases). However, the Raman data indicate formation of (Si-F)-bearing complexes, by substitution of F for O.

The presence of Si-F bonds were previously reported in SiO_2-NaF melts containing >7.5 mol% F (Mysen and Virgo 1985b). In addition, evidence of a small fraction of Si-F in silicate and aluminosilicate melts has been reported from ^{19}F NMR spectroscopy (Zeng and Stebbins 2000; Kiczenski et al. 2004; Kiczenski and Stebbins 2006). In a melt with a comparable NBO/T to those of this study (~0.4), Si-F complexes represent 90% of fluoride complexes (Mysen and Virgo 1985b). Therefore, two competing F solution mechanisms may occur in silicate melts: one involving the formation of M-F complexes, with M being an alkali such as Na or K, and the second being the formation of (Si-F)-bearing complexes:

$$2\ \text{Si-O-M} + F_2 \leftrightarrow \text{Si-O-Si} + 2\ \text{M-F} + \tfrac{1}{2}O_2 \quad (3a)$$
$$\text{Si-O-Si} + F_2 \leftrightarrow 2\ \text{Si-F} + \tfrac{1}{2}O_2. \quad (3b)$$

In Equations 3a and 3b, O_2 will be released by degassing. Equation 3a seems to dominate at low-F concentrations and results in a polymerization of the glass network, as observed by Mysen et al. (2004; F ~ 3 mol%). In contrast, Equation 3b appears to be more important at high-F concentrations (Mysen and Virgo 1985b; this study), and results in melt depolymerization (Fig. 6). An equilibrium between Si-F or M-F complexes at a given F concentration may be then described as:

$$\text{Si-F} + \text{Si-O-M} \leftrightarrow \text{M-F} + \text{Si-O-Si}. \quad (4)$$

Such an equilibrium reaction is likely dependent on F concentration, melt composition, pressure, and temperature conditions.

Fluorine in Al-bearing melts. Fluorine complexes with Al-F and Na-F bonding have been reported as the dominant solution mechanisms of F in anhydrous aluminosilicate melts (e.g., Schaller et al. 1992; Zeng and Stebbins 2000; Mysen et al. 2004; Baasner et al. 2014). The Al-F/Na-F abundance ratio increases with increasing Al/(Al+Si) of the melt (Mysen et al. 2004), which is consistent with increasing F solubility with increasing Al/(Al+Si) (Fig. 2). This is also consistent with the decreasing Raman signal assigned to Si-F bonds with increasing Al/(Al+Si) (Table 6). Therefore, in addition to fluorine reacting with Si-O-Si and Si-O-M bonds through the mechanisms described by Equations 3 and 4, F also can react with Si-O-Al bonds in aluminosilicate melts as:

$$\text{Si-O-Al} + F_2 \leftrightarrow \text{Si-F} + \text{Al-F} + \tfrac{1}{2}O_2 \quad (5a)$$
$$2\ \text{Si-O-Al} + F_2 \leftrightarrow \text{Si-O-Si} + 2\ \text{Al-F} + \tfrac{1}{2}O_2. \quad (5b)$$

As a result, in addition of Equation 4, two additional equilibria may exist between Si-F, Al-F, and M-F complexes:

$$\text{M-F} + \text{Si-O-Al} \leftrightarrow \text{Si-O-M} + \text{Al-F} \quad (6a)$$
$$\text{Si-F} + \text{Si-O-Al} \leftrightarrow \text{Si-O-Si} + \text{Al-F}. \quad (6b)$$

If Al^{3+} and its surrounding O and F atoms form fully neutral molecular species, Equations 5a and 5b may also imply that the alkali metals (here Na^+ or K^+), which were charge compensating Al^{3+} in tetrahedral coordination, become network modifiers. Consequently, Equations 5a and 5b may result in network depolymerization, potentially explaining increasing Q^2 and Q^3 fractions upon F addition in aluminosilicate glasses (Fig. 6).

The equilibrium constants of the above equations are unknown. However, existing data suggest that equilibria for solution mechanisms presented in Equations 3a, 3b, 5a, and 5b depend mostly on pressure (Fig. 2) and Al/(Al+Si) ratio (Fig. 3). The comparison of the various existing data reported above indicate that Equations 4a, 4b, 6a, and 6b, which define the coexistence of the various F-bearing complexes in the melt, have equilibrium constants depending on F concentration, melt chemical composition, and possibly temperature. Dalou and Mysen (2015) also

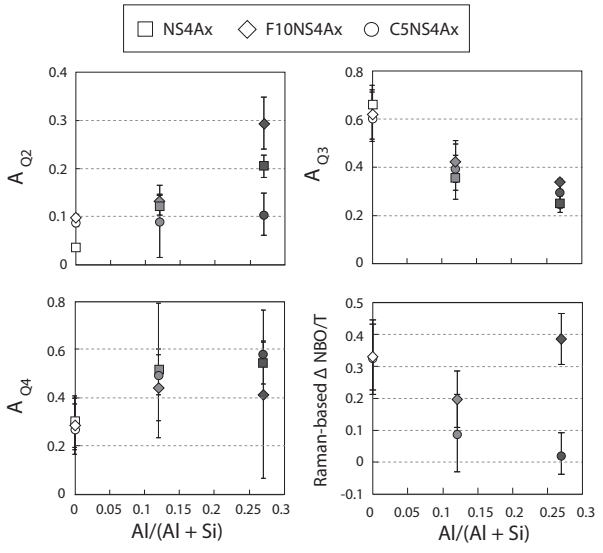

FIGURE 6. Relative area of the Raman signals assigned to (**a**) Q^2, A_{Q2}; (**b**) Q^3, A_{Q3}; and (**c**) Q^4, A_{Q4}, structural units of volatile-free (squares), F-bearing (diamonds), and Cl-bearing samples (circles). (**d**) Variation of melt polymerization, ΔNBO/T, with the addition of F and Cl, as a function of the bulk melt Al/(Al+Si) ratio. Increasingly darker symbols represent increasing Al/(Al+Si). Unit fractions of Q^n and ΔNBO/T are presented in Table 4.

show that Si-F complexes increase with increasing H_2O content dissolved in aluminosilicate melts.

Cl solution mechanisms

Chlorine in Al-free melts. It has been previously suggested that Cl dissolves in silicate melts by forming Cl-bearing complexes that contain Cl preferentially bonded to network-modifiers (Ca, Na, or K; e.g., Stebbins and Du 2002; Sandland et al. 2004; Zimova and Webb 2006; Evans et al. 2008; Baasner et al. 2013). Such a mechanism means that in Na-silicate melts, for example, formation of NaCl complexes results in a decrease in abundance of network-modifying Na^+, which results in silicate melt polymerization:

$$\text{Si-O-Na} + \text{Cl}_2 \leftrightarrow 2\ \text{Si-O-Si} + 2\text{NaCl} + \tfrac{1}{2}\text{O}_2. \quad (7)$$

Analogous expressions can be written for other alkali metals and alkaline earths. However, the Raman-based NBO/T of the C5NS4 glass is 0.32 higher than that of the pure NS4 glass (Table 6). The fractions of Q^4 and Q^3 decrease slightly and that of Q^2 increases in the C5NS4 glass compared to the pure NS4 glass (Table 6; Fig. 6). Moreover, an additional Raman peak is observed in the Cl-bearing glass near 890 cm^{-1}, which may be assigned to (Si,Al)-O^- vibrations in Q^1 structural units (cf. Mysen et al. 1982 and references therein). This peak does not contribute significantly to spectra (Fig. 5), but its appearance, as well as the increase of Q^2 fraction suggests an increase of melt depolymerization upon Cl solution.

Chlorine in Al-bearing melts. By increasing Al/(Al+Si) of Cl-saturated melts, Q^3 fraction decreases, whereas Q^4 fraction increases and Q^2 fraction remains constant, within error (Table 6, Fig. 6). In other words, Cl has a polymerizing effect in aluminosilicate melts. This effect increases with melt Al/(Al+Si) ratio (Fig. 6). This behavior can be explained with the aid of NaCl complexes, as described by Equation 7. As the melt Al/(Al+Si) increases, the bulk Q^3 fraction decreases (Fig. 6), and the solubility of Cl also decreases (Fig. 2). In addition, the ionic radius of alkali metals affects the solubility of Cl at a given Al/(Al+Si) ratio (Figs. 2 and 3). This suggests a control of the Cl solution behavior, and hence solubility, by the properties of network modifier metals together with their interaction with specific Q^n units.

Sandland et al. (2004), using ^{35}Cl NMR, estimated that up to 10% of the dissolved chlorine was in the form of Al-Cl or Si-Cl bonding in aluminosilicate melts. Although it cannot be asserted with certainty, we found no evidence of Si-Cl bonding in either Al-free or in Al-bearing melts.

Implications

Both the solubility of F and Cl in melts and their effect on melt structure are governed by the type of complexes formed with these halogens. The different solubility behavior (Fig. 2) may be related preferential bonding of F with Al and Si at high-F concentration through Equations 3b, 5a, and 5b, whereas Cl mainly bonds with network-modifying alkali cations. This difference also explains why Cl is more sensitive than F to the type of alkali (Na or K) in the melt (Fig. 2), although it remains unclear why Cl is more soluble in sodic systems than in potassic systems. It has been suggested that higher field strength cations ($Na^+ > K^+$) form more stable bonding with Cl^- (Stebbins and Zeng 2000). This behavior is consistent with Cl diffusivity data for phonolitic melts (Balcone-Boissard et al. 2009), which suggest that Cl interacts more strongly with Na than with K.

In Al-free melts, F and Cl have comparable solubility (within error, Fig. 2). In those melts, F causes depolymerization of the silicate structure, via formation of Si-F complexes. The chlorine solution mechanism seems also to cause depolymerization; the addition of Cl to silicate glass results an increase of Raman-based NBO/T and in the formation of highly depolymerized Q^1 and Q^2 units within the silicate network. The exact nature of the bonding of Cl in the present silicate melt remains unknown, but it is probable that Cl atoms reside in close proximity of the formed Q^1 and Q^2 units, where alkali metals will also be concentrated.

The addition of Al to silicate melts results in different relationships between dissolved halogen and aluminosilicate melt structure. Fluorine can react with the various Si-O-M, Si-O-Si, and Si-O-F bonds through different reactions with their equilibrium constants affected by the Al/(Al+Si) ratio of the melt, for instance. Indeed, the effect of F on the aluminosilicate melt structure depends primarily on the Na/Al ratio of the melt (Dingwell and Scarfe 1985; Dingwell 1989; Mysen et al. 2004), which determines the (Si,Al)-F/Na-F ratio. In contrast, Cl complexes mostly with network-modifiers, leading to melt polymerization. The effect of Cl on melt structure seems to rely mostly on its affinity to a specific alkali or alkali-earth cation, partly driving its solubility (Fig. 2).

It follows from the solution mechanisms of F and Cl that their effects on melt structure increase with Al/(Al+Si) content of magmas (Fig. 6). In terms of magma properties, this implies that the effect of F on magma viscosity increases from basaltic to felsic compositions. Furthermore, because several wt% F is soluble in Al-rich magma, fluorine can cause viscosity reduction of up to several orders of magnitude (as measured by Baasner et al. 2013), making it as efficient as H_2O in this regard (Dingwell and Mysen 1985). In contrast, Cl solubility decreases with increasing degree of magma differentiation [increasing Al/(Al+Si)]. Its influence on the rate of change of NBO/T with Al/(Al+Si) is smaller, therefore, than for F-bearing magma. It follows therefore that any magma property that depends on melt polymerization (e.g., viscosity, compressibility, element partitioning) is more sensitive to Al/(Al+Si) in F-rich magmatic systems than in Cl-rich systems. This is also observed in hydrous aluminosilicate melts in which H_2O melt depolymerization is more enhanced by F addition than by Cl addition (Dalou and Mysen 2015).

The effect of Cl on magma properties, however, does not simply depend on Al/(Al+Si) content. For example, Webb et al. (2014) show that Cl decreases the viscosity of iron-bearing aluminosilicate melts, whereas it increases the viscosity of iron-free aluminosilicate melts. This shows that the electronic properties of network former and network modifier elements play a strong role in determining the formation and stability of $M^{x}_{1/x}Cl$ complexes (with M a modifier element and x its electronic charge) within the silicate melt. This is corroborated by literature data that shows the influences of the molar $[Al_2O_3/(CaO+Na_2O+K_2O)]$, $[Na_2O/(Na_2O+K_2O)]$, and (Ca+Mg)/(Na+K) ratios of melts on the efficiency of Cl dissolution at fixed pressure conditions (Métrich and Rutherford 1992; Chevychelov and Chevychelova 1997; Signorelli and Carroll 2000). From an

extension of these relationships, Webster et al. (2015) compared the Cl solubility of fluid-saturated melts with increasing concentration of ($Ca^{1/2}$+$Mg^{1/2}$+$Al^{1/2}$+Na) and decreasing Si concentration in the melt for a range of *P-T* conditions. A very good agreement is found between Webster et al. (2015) model data and our experimental data of Cl solubility in Al-free melts with pressure.

From the above results and interpretations, it follows that the pressure (depth) at which halogens (both Cl and F) will be exsolved from a magmatic liquid is sensitive to the magma composition. For example, Al-rich magmas are likely to exsolve greater amounts of Cl than Al-poor magmas (Figs. 2 and 3). Consistently, Chevychelov and Suk (2003) have demonstrated that Cl solubility decreases by an order of magnitude as basaltic melts evolve to felsic compositions and that Cl partitions increasingly in favor of fluids as magmas evolve from mafic to felsic residual melt compositions.

Acknowledgments

This research was conducted with partial support from NSF grant EAR-1212754 (to B.O.M. and C.D.), and NAI grant to the Geophysical Laboratory. We acknowledge very helpful reviews by Associate Editor Grant Henderson, Hélène Balcone-Boissard, and one anonymous reviewer, which considerably improve this manuscript. We thank Robert Dennen for his help with English edits. We also thank J.T. Armstrong and K. Crispin for their help with the optimization of the SEM/EDS analytical protocol.

References cited

Alletti, M., Baker, D.R., and Freda, C. (2007) Halogen diffusion in a basaltic melt. Geochimica et Cosmochimica Acta, 71, 3570–3580.

Allwardt, J.R., Poe, B.T., and Stebbins, J.F. (2005) The effect of fictive temperature on Al coordination in high-pressure (10 GPa) sodium aluminosilicate glasses. American Mineralogist, 90, 1453–1457.

Baasner, A., Schmidt, B.C., and Webb, S.L. (2013) Compositional dependence of the rheology of halogen (F, Cl) bearing-aluminosilicate melts. Chemical Geology, 346(C), 172–183.

Baasner, A., Hung, I., Kemp, T.F., Dupree, R., Schmidt, B.C., and Webb, S.L. (2014) Constraints on the incorporation mechanism of chlorine in peralkaline and peraluminous Na_2O-CaO-Al_2O_3-SiO_2 glasses. American Mineralogist, 99, 1713–1723.

Balcone-Boissard, H., Baker, D.R., Villemant, B., and Boudon, G. (2009) F and Cl diffusion in phonolitic melts: Influence of the Na/K ratio. Chemical Geology, 263, 89–98.

Balcone-Boissard, H., Boudon, G. and Villemant, B. (2011) Textural and geochemical constraints on eruptive style of the 79 AD eruption at Vesuvius. Bulletin of Volcanology, 73, 279–294.

Bohlen, S.R. (1984) Equilibria for precise pressure calibration and a frictionless furnace assembly for the piston-cylinder apparatus. Neues Jahrbuch für Mineralogie, Monatshefte, 84, 404–412.

Böhm, A., and Schmidt, B.C. (2013) Fluorine and chlorine diffusion in phonolitic melt. Chemical Geology, 346, 162–171.

Boyd, F.R., and England, J.L. (1960) Apparatus for phase equilibrium measurements at pressures up to 50 kilobars and temperatures up to 1750°C. Journal of Geophysical Research, 65, 741–748.

Chevychelov, V.Y., and Chevychelova, T.K. (1997) Partitioning of Pb, Zn, W, Mo, CI, and major elements between aqueous fluid and melt in the systems granodiorite (granite, leucogranite)-H_2O-NaCl-HCl. Neues Jahrbuch für Mineralogie-Abhandlungen, 101–115.

Chevychelov, V.Y., and Suk, N.I. (2003) Influence of the composition of magmatic melt on the solubility of metal chlorides at pressures of 0.1-3.0 kbar. Petrology, 11, 62–74.

Chevychelov, V.Y., Bocharnikov, R.E., and Holtz, F. (2008) Experimental study of chlorine and fluorine partitioning between fluid and subalkaline basaltic melt. Doklady Earth Sciences, 422(1), 1089–1092.

Dalou, C., and Mysen, B.O. (2015) The effect of H_2O on F and Cl solubility and solution mechanisms of in aluminosilicate melts at high pressure and high temperature. American Mineralogist, 100, 633–643.

Dingwell, D.B. (1987) Melt viscosities in the system $NaAlSi_3O_8$-H_2O-F_2O_{-1}. In B.O. Mysen, Ed., Magmatic Processes: Physicochemical Principles, pp. 423–432. The Geochemical Society, Washington, D.C.

——— (1989) Effect of fluorine on the viscosity of diopside liquid. American Mineralogist, 74, 333–338.

Dingwell, D.B., and Hess, K.U. (1998) Melt viscosities in the system Na-Fe-Si-O-F-Cl: Contrasting effects of F and Cl in alkaline melts. American Mineralogist, 83, 1016–1021.

Dingwell, D.B., and Mysen, B.O. (1985) Effects of water and fluorine on the viscosity of albite melt at high pressure: a preliminary investigation. Earth and Planetary Science Letters, 74, 266–274.

Dingwell, D.B., and Scarfe, C.M. (1985) Chemical diffusion of fluorine in melts in the system Na_2O-Al_2O_3-SiO_2. Earth and Planetary Science Letters, 73, 377–384.

Dingwell, D.B., Knoche, R., and Webb, S.L. (1993) The effect of F on the density of haplogranite melt. American Mineralogist, 78, 325–330.

Dumas, P., Corset, J., Carvalho, W., Levy, Y., and Neuman, Y. (1982) Fluorine-doped vitreous silicate analysis of fiber optics preforms by vibrational spectroscopy. Journal of Non-Crystalline Solids, 47, 239–242.

Duncan, T.M., Douglass, D.C., Csenscits, R., and Walker, K.L. (1986) Study of fluorine in silicate glasses with ^{19}F nuclear magnetic resonance spectroscopy. Journal of Applied Physics, 60, 130–136.

Evans, K.A., Mavrogenes, J.A., O'Neill, H.S., Keller, N.S., and Jang, L.Y. (2008) A preliminary investigation of chlorine XANES in silicate glasses. Geochemistry Geophysics Geosystems, 9, Q10003, http://dx.doi.org/10.1029/2008GC002157.

Efron, B., and Tibshirani, R. (1994) An Introduction to the Bootstrap. Monographs on Statistics and Applied Probability 57, Chapman & Hall/CRC Press, Florida.

Filiberto, J., and Treiman, A.H. (2009) The effect of chlorine on the liquidus of basalt: First results and implications for basalt genesis on Mars and Earth. Chemical Geology, 263, 60–68, http://dx.doi.org/10.1016/j.chemgeo.2008.08.025.

Filiberto, J., Wood, J., Dasgupta, R., Shimizu, N., Le, L., and Treiman, A.H. (2012) Effect of fluorine on near-liquidus phase equilibria of an Fe–Mg rich basalt. Chemical Geology, 312-313, 118–126.

Foley, S.F., Taylor, W.R., and Green, D.H. (1986) The effect of fluorine on phase relationships in the system $KAlSiO_4$-Mg_2SiO_4-SiO_2 at 28 kbar and the solution mechanism of fluorine in silicate melts. Contributions to Mineralogy and Petrology, 93, 46–55.

Giordano, D., Romano, C., Dingwell, D.B., Poe, B., and Behrens, H. (2004) The combined effects of water and fluorine on the viscosity of silicic magmas. Geochimica et Cosmochimica Acta, 68, 5159–5168.

Hardy, J.R., Karo, A.M., Morrsion, I.W., Sennett, C.T., and Russell, J.P. (1969) Lattice dynamics and second-order Raman spectrum of NaF. Physical Review, 179, 837.

Jago, B.C., and Gittins, J. (1989) Silver fluoride (AgF) as source of fluorine in experimental petrology. American Mineralogy, 74, 936–937.

Jones E., Oliphant, E., Peterson, P., and others. (2001) SciPy: Open Source Scientific Tools for Python, http://www.scipy.org/, accessed August 2014.

Kiczenski, T.J., and Stebbins, J.F. (2006) The effect of fictive temperature on the structural environment of fluorine in silicate and aluminosilicate glasses. Journal of the American Ceramic Society, 89, 57–64.

Kiczenski, T.J., Du, L.S., and Stebbins, J.F. (2004) F-19 NMR study of the ordering of high field strength cations at fluoride sites in silicate and aluminosilicate glasses. Journal of Non-Crystalline Solids, 337, 142–149.

Kohn, S.C., Dupree, R., Mortuza, M.G., and Henderson, C.M.B. (1991) NMR evidence for five- and six- coordinated aluminum fluoride complexes in F-bearing aluminosilicate glasses. American Mineralogist, 76, 309–312.

Kuisma-Kursula, P. (2000) Accuracy, precision and detection limits of SEM-WDS, SEM-EDS and PIXE in the multi-elemental analysis of medieval glass. X-ray Spectrometry, 29, 111–118.

Kushiro, I. (1976) A new furnace assembly with a small temperature gradient in solid-media, high-pressure apparatus. Carnegie Institution Washington Yearbook, 75, 832–833.

Le Losq, C., and Neuville, D.R. (2013) Effect of the Na/K mixing on the structure and the rheology of tectosilicate silica-rich melts. Chemical Geology, 346, 57–71.

Le Losq, C., Neuville, D.R., Florian, P., Henderson, G.S., and Massiot, D. (2014) The role of Al^{3+} on rheology and structural changes in sodium silicate and aluminosilicate glasses and melts. Geochimica et Cosmochimica Acta, 126, 495–517.

Luth, R.W. (1988a) Effects of F on phase equilibria and liquid structure in the system $NaAlSiO_4$-$CaMgSi_2O_6$-SiO_2. American Mineralogist, 73, 306–312.

——— (1988b) Raman spectroscopic study of the solubility mechanisms of F in glasses in the system CaO-CaF_2-SiO_2. American Mineralogist, 73, 297–305.

Matson, D.W., Sharma, S.K., and Philpotts, J.A. (1986) Raman spectra of some tectosilicates and of glasses along the orthoclase-anorthite and nepheline-anorthite joins. American Mineralogist, 71, 694–704.

McMillan, P. (1984) A Raman spectroscopic study of glasses in the system CaO-MgO-SiO_2. American Mineralogist, 69, 645–659.

Merzbacher, C.I., and White, W.B. (1991) The structure of alkaline earth aluminosilicate glasses as determined by vibrational spectroscopy. Journal of Non-Crystalline Solids, 130, 18–34.

Métrich, N., and Rutherford, M.J. (1992) Experimental study of chlorine behavior in hydrous silicic melts. Geochimica et Cosmochimica Acta, 56, 607–616.

Mysen, B.O. (1990) Relationships between silicate melt structure and petrologic processes. Earth-Science Reviews, 27, 281–365.

——— (1999) Structure and properties of magmatic liquids: From haplobasalt to haploandesite. Geochimica et Cosmochimica Acta, 63, 95–112.

——— (2007) The solution behavior of H_2O in peralkaline aluminosilicate melts at high pressure with implications for properties of hydrous melts. Geochimica et Cosmochimica Acta, 71, 1820–1834.

Mysen, B.O., and Cody, G.D. (2001) Silicate-phosphate interactions in silicate glasses and melts: II. Quantitative, high-temperature structure of P-bearing alkali aluminosilicate melts. Geochimica et Cosmochimica Acta, 65, 2413–2431.

——— (2005) Solution mechanisms of H_2O in depolymerized peralkaline melts.

Geochimica et Cosmochimica Acta, 69, 5557–5566.
Mysen, B.O., and Frantz, J.D. (1993) Structure of silicate melts at high temperature: In-situ measurements in the system BaO-SiO_2 at 1669°C. American Mineralogist, 78, 699–709.
Mysen, B.O., and Richet, P. (2005) Silicate Glasses and Melts, Properties and Structure. Elsevier, Amsterdam.
Mysen, B.O., and Virgo, D. (1985a) Structure and properties of fluorine-bearing aluminosilicate melts: the system Na_2O-Al_2O_3-SiO_2-F at 1 atm. Contributions to Mineralogy and Petrology, 91, 205–220.
——— (1985b) Interaction between fluorine and silica in quenched melts on the joins SiO_2-AlF_3 and SiO_2-NaF determined by Raman spectroscopy. Physics and Chemistry of Minerals, 12, 77–85.
Mysen, B.O., Finger, L.W., Virgo, D., and Seifert, F.A. (1982) Curve-fitting of Raman spectra of silicate glasses. American Mineralogist, 67, 686–695.
Mysen, B.O., Lucier, A., and Cody, G.D. (2003) The structural behavior of Al^{3+} in peralkaline melts and glasses in the system Na_2O-Al_2O_3-SiO_2. American Mineralogist, 88, 1668–1678.
Mysen, B.O., Cody, G.D., and Smith, A. (2004) Solubility mechanisms of fluorine in peralkaline and meta-aluminous silicate glasses and in melts to magmatic temperatures. Geochimica et Cosmochimica Acta, 68, 2745–2769.
Nelder, J.A., and Mead, R. (1965) A simplex method for function minimization. Computer Journal, 7, 308–313.
Neuville, D.R. (2006) Viscosity, structure and mixing in (Ca, Na) silicate melts. Chemical Geology, 229, 28–41.
Neuville, D.R., and Mysen, B.O. (1996) Role of aluminium in the silicate network: In situ, high-temperature study of glasses and melts on the join SiO_2-$NaAlO_2$. Geochimica et Cosmochimica Acta, 60, 1727–1737.
Neuville, D.R., Hennet, L., Florian, P., and de Ligny, D. (2014) In situ high-temperature experiments. Reviews in Mineralogy and Geochemistry, 78, 779–800.
Newville, M., Stensitzki, T., Allen, D.B., and Ingargiola, A. (2014) LMFIT: Non-Linear Least-Square Minimization and Curve-Fitting for Python¶. Zenodo, http://dx.doi.org/10.5281/zenodo.11813.
Osborn, E.F, and Muan, A. (1960) Phase equilibrium diagrams for ceramists. Plate 4. The system Na_2O-Al_2O_3-SiO_2. American Ceramic Society, Columbus, Ohio.
Pasquarello, A., Sarnthein, J., and Car, R. (1998) Dynamic structure factor of vitreous silica from first principles: Comparison to neutron-inelastic-scattering experiments. Physical Review B, 57, 14133.
Powell, M.J.D. (1964) An efficient method for finding the minimum of a function of several variables without calculating derivatives. Computer Journal, 7, 155–162.
Raudsepp, M. (1995) Recent advances in the electron micro-analysis of minerals for the light elements. Canadian Mineralogist, 33, 203–218.
Sandland, T.O., Du, L.-S., Stebbins, J.F., and Webster, J.D. (2004) Structure of Cl-containing silicate and aluminosilicate glasses: A ^{35}Cl MAS-NMR study. Geochimica et Cosmochimica Acta, 68, 5059–5069.
Sarnthein, J., Pasquarello, A., and Car, R. (1997) Origin of the high-frequency doublet in the vibrational spectrum of vitreous SiO_2. Science, 275, 1925–1927.
Schaller, T., Dingwell, D.B., Keppler, H., Knöller, W., Merwin, L., and Sebald, A. (1992) Fluorine in silicate glasses: A multinuclear nuclear magnetic resonance study. Geochimica et Cosmochimica Acta, 56, 701–707.
Seifert, F., Mysen, B.O., and Virgo, D. (1982) Three-dimensional network structure of quenched melts (glass) in the systems SiO_2-$NaAlO_2$, SiO_2-$CaAlO_4$ and SiO_2-$MgAl_2O_4$. American Mineralogist, 67, 696–717.
Signorelli, S., and Carroll, M.R. (2000) Solubility and fluid-melt partitioning of Cl in hydrous phonolitic melts. Geochimica et Cosmochimica Acta, 64, 2851–2862.
Spiekermann, G., Steel-McInnis, M., Schmidt, C., and Jahn, S. (2012) Vibrational mode frequencies of silica species in SiO_2-H_2O liquids and glasses from ab initio molecular dynamics. The Journal of Chemical Physics, 136, 154501.
Spiekermann, G., Steele-MacInnis, M., Kowalski, P.M., Schmidt, C., and Jahn, S. (2013) Vibrational properties of silica species in MgO-SiO_2 glasses obtained from ab initio molecular dynamics. Chemical Geology, 346, 22–33.
Stagno, V., and Dolejš, D. (2007) Chlorine solubility in polymerized aluminosilicate melts. Bayerisches Geoinstitut Annual Report 2007, 137–140.
Stebbins, J.F., and Du, L.-S. (2002) Chloride ion sites in silicate and aluminosilicate glasses: A preliminary study by ^{35}Cl solid-state NMR. American Mineralogist, 87, 359–363.
Stebbins, J.F., and Zeng, Q. (2000) Cation ordering at fluoride sites in silicate glasses: a high-resolution ^{19}F NMR study. Journal of Non-Crystalline Solids, 262, 1–5.
Stebbins, J.F., Kroeker, S., and Lee, S.K. (2000) Quantification of five- and six-coordinated aluminum ions in aluminosilicate and fluoride-containing glasses by high-field, high-resolution ^{27}Al NMR. Journal of Non-Crystalline Solids, 275, 1–6.
Stelling, J., Botcharnikov, R.E., Beermann, O., and Nowak, M. (2008) Solubility of H_2O and chlorine-bearing fluids in basaltic melt of Mount Etna at T= 1050–1250° C and P= 200 MPa. Chemical Geology, 256, 102–110.
van Groos, A.F.K., and Wyllie, P.J. (1968) Melting relationships in the system $NaAlSi_3O_8$-NaF-H_2O to 4 kilobars pressure. The Journal of Geology, 76, 50–70.
Villemant, B., and Boudon, G. (1998) Transition from dome-forming to plinian eruptive styles controlled by H_2O and Cl degassing. Nature, 392, 65–69.
Webb, S.L., Murton, B.J., and Wheeler, A.J. (2014) Rheology and the Fe^{3+}–chlorine reaction in basaltic melts. Chemical Geology, 366, 24–31.
Webster, J.D., and De Vivo, B. (2002) Experimental and modeled solubilites of chlorine in aluminosilicate melts, consequences of magma evolution, and implications for exsolution of hydrous chloride melt at Mt. Somma-Vesuvius. American Mineralogist, 87, 1046–1061.
Webster, J.D., Vetere, F., Botcharnikov, R.E., Goldoff, B., McBirney, A., and Doherty, A.L. (2015) Experimental and modeled chlorine solubilities in aluminosilicate melts at 1 to 7000 bars and 700 to 1250 °C: Applications to magmas of Augustine Volcano, Alaska. American Mineralogist, 100, 522–535.
Woltring, H.J. (1986) A FORTRAN package for generalized, cross-validator spline smoothing and differentiation. Advances in Engineering Software, 8, 104–113.
Wyllie, P.J., and Tuttle, O.F. (1961) Experimental investigation of silicate systems containing two volatile components. American Journal of Science, 259, 128–143.
Yamamoto, K., Nakanishi, T., Kasahara, H., and Abe, K. (1983) Raman scattering of SiF4 molecules in amorphous fluorinated silicon. Journal of Non-Crystalline Solids, 59-60, 213–216.
Zeng, Q., and Stebbins, J.F. (2000) Fluoride sites in aluminosilicate glasses: High-resolution ^{19}F NMR results. American Mineralogist, 85, 863–867.
Zimova, M., and Webb, S.L. (2006) The effect of chlorine on the viscosity of Na_2O-Fe_2O_3-Al_2O_3-SiO_2 melts. American Mineralogist, 91, 344–352.
——— (2007) The combined effects of chlorine and fluorine on the viscosity of aluminosilicate melts. Geochimica et Cosmochimica Acta, 71, 1553–1562.

Manuscript received September 25, 2014
Manuscript accepted April 15, 2015
Manuscript handled by Grant Henderson